Journal of Membrane Science 464 (2014) 161–172

Contents lists available at ScienceDirect

Journal of Membrane Science

journal homepage: www.elsevier.com/locate/memsci

Analysis of forward osmosis desalination via two-dimensional FEM model

Abraham Sagiv [a], Aihua Zhu [b], Panagiotis D. Christofides [b], Yoram Cohen [b], Raphael Semiat [a,*]

[a] Wolfson Faculty of Chemical Engineering, Technion – Israel Institute of Technology, Technion City, Haifa 32000, Israel
[b] Department of Chemical and Biomolecular Engineering, University of California, Los Angeles, CA, USA

ARTICLE INFO

Article history:
Received 22 June 2013
Received in revised form
27 March 2014
Accepted 1 April 2014
Available online 13 April 2014

Keywords:
Desalination
Forward osmosis
Mass transfer
FEM modeling
Concentration polarization

ABSTRACT

Forward osmosis (FO) desalination was investigated via 2-D numerical model of the fully coupled hydrodynamics and mass transfer equations. The model was formulated for a detailed composite channel structure (feed and draw channels, membrane skin layer and porous support) being capable of describing co-current or counter current cross operation where the membrane skin faces the salt feed solution (SFF) or where the membrane skin faces the draw solution (SFD). Simulations based on existing experimental FO data confirmed that FO operation in a counter-current/SFD mode provides slight improvement with respect to water flux, and reduced cross migration of feed and draw solutes relative to the co-current mode of operation. Analysis of existing FO data also revealed the dependence of the intrinsic membrane water permeability and solute transport coefficients on draw solute concentration. Simulation results indicated significant cross membrane migration of feed and draw solutes for long (~1 m) relative to short (~10 cm) FO channels. Moreover, up to an order of magnitude decline of draw solute concentration difference (along the membrane) can be encountered at the draw channel exit region. Simulation results suggest that accurate assessment of FO performance in long channels is critical for full-scale plant design in order to minimize salt leakage, optimize recovery, and setting accurate inlet/outlet conditions to enable simulations of membrane elements in series.

1. Introduction

Forward osmosis (FO) desalination is a process in which a high osmotic pressure draw solution, on the permeate side of a semi-permeability membrane, serves to draw water from an aqueous solution (usually a saline solution) of lower osmotic pressure on the feed side of the membrane channel. Depending on the specific FO application, the feed solution can be seawater, treated wastewater [1], brackish water [2], and polluted water [3] or even distilled water for RO backwash or experimental studies and process characterization. The selection of an effective draw solution represents a significant challenge [4]. The draw solution should be of a sufficiently high osmotic pressure to maximize the water flux drawn from the feed to the draw solution side. When potable water production is the goal, subsequent to desalination, the draw solution must be treated (i.e. purified) to remove the solute responsible for its high osmotic pressure, thereby producing potable desalted water. A detailed description of the FO process and its various actual and potential applications is provided in [5]. Various draw solutes have been investigated such as KCl, $NaNO_3$ and KNO_3 [4,6], and NH_4HCO_3 [4]. During the FO process, concentration differences across the membrane for the feed and draw solutes can result in solute cross-migration [7,8]. As a consequence, draw solute which could diffuse to the feed side of the membrane channel may be lost in the concentrate stream, if not recovered. Also, salt ions that diffuse from the feed-side to the draw-solution will reduce the quality of the produced permeate and could also negatively impact reclamation of the draw solute. Moreover, the permeate water stream dilutes the draw solute concentration, while the salt concentration increases axially in the membrane channel. The draw solution may be further diluted due to draw solute cross-migration from the draw to the feed channel. Depending on the intended use of the product water (which may contain the draw solute, unless it is removed by an additional separation process) draw solute/solution make-up may be needed in order to compensate for losses during both draw solution regeneration and draw solute loss due to cross-migration [4].

In an effort to better understand the FO process, various analytical and numerical transport models have been proposed [9–13, 14]. The majority of published FO models are derivatives of the

* Corresponding author. Tel./fax: +972 4829 2009.
E-mail address: cesemiat@tx.technion.ac.il (R. Semiat).

http://dx.doi.org/10.1016/j.memsci.2014.04.001
0376-7388/

solution-diffusion and film models and thus are based on the assumption of fully-developed concentration and flow fields. These one-dimensional models do not consider axial development of the flow and concentration profiles along the membrane channel and typically assume concentration invariant transport parameters. Also, the above modeling approaches introduce mass transfer coefficients (in the feed and draw channels) as lumped parameters extracted from experimental data or derived from empirical correlations (e.g., Sherwood number as a function of the Reynolds and Schmidt numbers) [9,15–17]. Despite its simplicity, the 1-D modeling approach has provided a convenient means of accounting for the effects of internal and external concentration polarization (CP) layers on water flux [16]. Such models have provided a framework that has been extended to modeling of pressure retarded osmosis whereby pressure is applied on the draw solution side [18].

A fully-developed one dimensional (1-D) analytical mass transfer model was developed to account for a special case of backwash (BW) cleaning of reverse osmosis (RO) membranes [14] that can be considered as a special case of FO desalination with zero cross flow velocity (on the channel permeate side). A numerical model, based on one dimensional (1-D) mass balance, along and across each of the feed and draw channels, was also developed [19] to account for performances of various FO configurations. A two-dimensional (2D) flow and mass transfer FEM model was also developed [12,20] to account for a general case of the backwash (BW) cleaning of RO membranes. Two-dimensional simulations were conducted [21] to account for the effects of external and internal CP layers (ECP and ICP, respectively) with the two membrane orientations with respect to water flux. More recently, steady-state 2-D FEM FO models involving the coupled momentum and mass transfer equations were developed to account for a single solute FO desalination and evaluated for test cases based on NaCl solutions [13,22]. These models involve solving the coupled mass and momentum transfer equations with boundary conditions appropriate for FO desalination with water/NaCl and NaCl/NaCl solutions in the feed/draw channels, respectively. It was reported that reduction in water flux is primarily due to increased mass resistance due to dilution of the draw-side CP layer [13] or ECP [22], in addition to membrane skin layer resistance. It was also reported [13] that the degree of flux reduction due to the porous membrane support (due to ICP) is significantly lower relative to that of the draw solution ECP layer. Previous findings have suggested that minimization of the skin thickness and the draw-side CP layer resistances to water permeation are more significant than minimization of the membrane ICP porous support resistance. Similar conclusions as to the dominancy of the draw ECP, in affecting the reduction in permeate flux, were arrived by [22,23] based on simulations with a 2-D CFD model integrated with 1-D film model. Also, the 2-D FO models that have been proposed in recent years [13,24], including those dealing with the role of channel spacers [25], have focused on simulations for same solute on both sides of the FO membrane. It is also noted that results from a recent CFD modeling study [25] (using NaCl for both draw and feed salts) revealed that ICP dominance was attained only when an artificially high support layer thickness was assumed ($\sim$10 times the typical support layer thickness of $\lesssim$0.1 mm).

The use of different feed and draw solutes in FO is expected to be accompanied by cross-migration (i.e., across the FO membrane) of the draw and feed solute pairs (from feed to draw and draw to feed sides), given that at present FO membranes do not provide complete solute rejection. Solute cross-migration and the ensuing impacts on FO process performance is likely to be more pronounced with increased membrane channel length. Accordingly, in the present work, a general 2-D FO model was developed and simulations were carried out to assess the impact of solute cross-migration and channel length on FO performance. Numerical finite-element FO simulations (based on the fully-coupled hydrodynamics and mass transfer equations) were carried out focusing on test cases for NaCl, NH_4HCO_3, and KCl as draw solutes with aqueous NaCl solutions as the feed. Membrane parameters, extracted from experimental data using the FO model, were subsequently utilized to investigate, using a 2-D model of the fully-coupled hydrodynamics and mass transfer (for both feed salt and draw solutes) equations, the flow hydrodynamics and concentration fields in both typical short (laboratory-type) and long FO channels. Simulation results then served to evaluate, for the above channel types, solute cross-migration (i.e. leakage of feed and draw salts) in relation to permeate flux and recovery, as well as channel outlet salt and draw solute concentrations.

2. Model development

A numerical 2-D FEM FO desalination model was developed for the FO system shown in Fig. 1 in which the half channels are shown on both sides of a skin membrane supported by a porous membrane layer. The present FO model formulation, which consists of the fully-coupled hydrodynamics (Navier–Stokes) and mass transfer transport equations, extends previous work [13] by accounting for the presence of different solute species in the feed and draw solutions, while also accounting for the concentration-dependence of the relevant transport properties. FO desalting is modeled (Fig. 1) for feed solution flowing in a channel *f* (usually NaCl solution) with NH_4HCO_3, KCl or other appropriate solute (in the draw solution side), flowing in an adjoining channel *d*. The lateral coordinate is *x* and *y* is the coordinate along the membrane length, whereby the concentration polarization (CP) layers develop axially (in the y direction) along the membrane surface (on both the draw and feed sides).

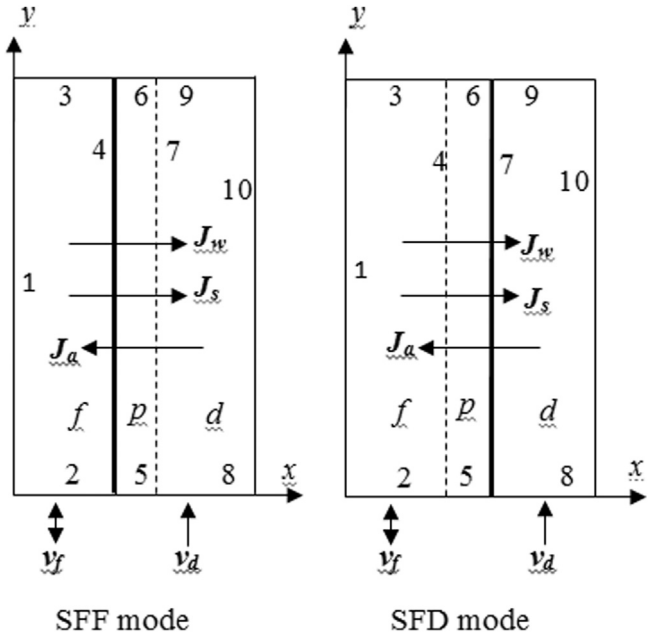

Fig. 1. Forward osmosis channel domains for two different configurations with NaCl in the feed channel (*f*) and NH_4HCO_3 (or KCl) in the draw channel (*d*): (Left) Skin faced feed (SFF) mode in which the skin (or active layer indicated by the bold vertical line) faces the salt (NaCl) solution in the feed-side, (Right) skin faced draw (SFD) mode in which the draw solute faces the skin side in the draw channel. Porous support is denoted by *p* and the cross flow velocities are denoted by *v*. The domain boundaries are numbered 1–10. Fluxes of water, NaCl and NH_4HCO_3 (or KCl) are denoted by J_w, J_s and J_a, or J_k, respectively, and *x*, *y* are the lateral (traverse) and axial (along the membrane channel length), respectively. Co-current and counter-current modes are defined when v_f is from bottom or the top, respectively.

Two membrane orientations are shown in Fig. 1: (a) skin (or active layer, the bold vertical line shown in the figure) faced feed (SFF) mode, and (b) skin faced draw (SFD) mode, with the porous support denoted by p. Cross flow velocities are denoted by v, and co-current and counter-current modes are defined in the figure when v_f is designated with either an up or down arrow, respectively. The presented modeling scheme can thus be used to simulate FO with different feed and draw solutes, and for handling different operational modes such as SFF, SFD, co-current and counter-current cross flows. Fluxes of water, NaCl and NH_4HCO_3 (or KCl) are indicated in Fig. 1 by J_w, J_s and J_a, respectively. Irrespective of the operational mode, water permeation flux (from the feed to draw side) is expected to decrease axially along the channel since the osmotic pressure driving force (across the membrane) decreases progressively. Water flux from the feed to the draw channel dilutes the draw concentration at the membrane surfaces (dilutive CP), while leading to increased (feed) salt concentration on the feed side of the membrane (concentrative CP). Given the above, 2-D simulations are necessary in order to properly assess the implications of the above CP layers, particularly with respect to FO process performance expected in long commercial FO channels.

Specific membrane properties were utilized in demonstrating the application of the model and interpretation of available experimental data. Specifically, calculations of the flow field require the following four input parameters: solution density (ρ), dynamic viscosity (η), solute diffusivity (D) and osmotic pressure of the solution at the appropriate concentration (π). Membrane permeability for the transport of water and solutes (i.e., salts) across the membrane are also required. These permeabilities are denoted here as A for water, and B_s and B_a for NaCl and NH_4HCO_3 (or KCl) solutions, respectively. Finally, it is noted that numerical solution of the model equations requires specification of the boundary conditions for cross flow velocities and concentrations, for both the feed and draw solution channels, for the 10 boundaries (Fig. 1) in three domains: the two half channels and the porous membrane support as specified in Table 1.

2.1. Fluid flow equations

Steady-state flow through the FO channels is described by the momentum and continuity equations [26];

$$\rho_i \mathbf{u}_i \cdot \nabla \mathbf{u}_i = -\nabla p_i + \nabla \cdot \eta_i (\nabla \mathbf{u}_i + (\nabla \mathbf{u}_i)^T), \quad \nabla \cdot \mathbf{u}_i = 0 \tag{1}$$

Eq. (1) describes 2-D flow in both feed ($i=f$) and draw ($i=d$) channels along x and y coordinates, respectively, ρ, η and p, are the solutions density, dynamic viscosity and pressure, respectively, $\nabla \equiv (\partial/\partial x, \partial/\partial y)$ is a 2-D operator of derivatives along x and y coordinates, respectively, and $\mathbf{u} \equiv (u, v)$ is the velocity vector along the x, y coordinates, respectively. The flow field within the porous support is described by Brinkman's equation [26],

$$\frac{\eta}{\kappa}\mathbf{u} = -\nabla p + \frac{1}{\varepsilon_p}\nabla \cdot \eta(\nabla \mathbf{u} + (\nabla \mathbf{u})^T), \quad \nabla \cdot \mathbf{u} = 0 \tag{2}$$

where κ and ε_p are the permeability and porosity of the porous support respectively. Eq. (2) is applicable for isotropic supports. However, for anisotropic supports (e.g., supports with straight through pores) Eq. (2) remains valid but with the permeability taken to be a tensor. The flow regime in both channels is laminar [27,28] and thus the velocity profile at the entrance (i.e., $y=0$) was taken to be parabolic, while the axial velocity in the support layer at $y=0$, L was taken to be zero.

2.2. Solute convection and diffusion

Solute transport in the FO system is the result of convection and Fickian diffusion due to local concentration gradients within the solutions and across the membrane. Solute transport within both half channels can be described by the convection-diffusion equation [26],

$$\nabla \cdot (D_{k:i} \nabla c_{k,i}) = \mathbf{u}_{k,j} \cdot \nabla c_{k,i} \tag{3}$$

in which the index k is designated as f, p or d for the feed, porous support and draw domains, respectively, and j designates the components of the velocity vector $\mathbf{u}$ along x and y coordinates. The index i in Eq. (3) can be designated as $i=a$, or s, for NH_4HCO_3 (or KCl) and NaCl, respectively. The effective solute diffusivity in the porous support depends on membrane orientation. In the SFF mode, the effective solute diffusivity is $\varepsilon_p D_i/\tau$, where i is the draw solute (i.e., subscript a; Table 1) in the SFD mode and the feed salt solute is designated by s (Table 1), and τ is the tortuosity of the membrane support layer. Eq. (3) is applicable to each of the solutes in a multicomponent system. For FO with two different salt and draw solutes, passage of these salts across the membrane (i.e., feed salt to the draw side and draw salt to the feed side) will result in binary salt solutions on either side of the membrane. However, concentrations of the feed salt and draw salt in the draw and feed channels, respectively, are expected to be sufficiently low (as revealed by the numerical simulations, Section 3) to justify the neglect of binary salt interactions

Table 1
Boundary conditions for various FO system configurations (SFF and SFD) and co-current and counter-current cross flow modes of operation.

Boundary	Navier–Stokes			Solute convection and diffusion		
	Feed	Porous	Draw	Feed	Porous	Draw
1[b]	Impermeable, no-slip			Impermeable		
2 Counter-current	Outlet[a]			Convective flux		
2 Co-current	inlet v_f			C_{af0} and C_{sf0}		
3 Counter-current	Outlet[a]			C_{af0} and C_{sf0}		
3 Co-current	Inlet v_f			Convective flux		
4 (SFF)	Outlet J_w	Inlet J_w		Outlet J_s, inlet J_a	Inlet J_s, outlet J_a	
4 (SFD)	Outlet J_w	Inlet J_w		$c_{af}=c_{ap}$; $c_{sf}=c_{sp}$	$c_{ap}=c_{af}$; $c_{sp}=c_{sf}$	
5		Wall			Insulation	
6		Wall				
7 (SFF)		Outlet[a]	Inlet J_w		$c_{ap}=c_{ad}$; $c_{sp}=c_{sd}$	$c_{ad}=c_{ap}$; $c_{sd}=c_{sp}$
7 (SFD)		Outlet[a]	Inlet J_w		Outlet J_s inlet J_a	Inlet J_s outlet J_a
8			Inlet v_d			C_{ad0} and C_{sd0}
9			Outlet[a]			Convective flux
10[b]			Impermeable, no-slip			Impermeable

[a] At the outlet, both pressure and viscous stresses vanish; Note: subscript $i=s$ or a designate the feed salt and draw solute, respectively, and subscripts f and d designate feed and draw channel sides, respectively.

[b] Note that for the long channels where a feed channel is bounded by two draw channels, as in a spiral wound membrane unit, boundaries (1) and (10) can be taken to be planes of symmetry with respect to the traverse coordinate without invoking the longitudinal no-slip condition.

when estimating the mass diffusion coefficients as well as the negligible impact on the solution density and viscosity.

Boundary conditions for the concentrations of the solutions at the entrance to the draw and feed channels are C_{ad} and C_{sf}, respectively. Entrance uniform bulk concentrations across the channels are designated as C_{ad}, C_{sf}, and zero within the draw, feed and porous support, respectively. The set of boundary conditions for the FO system for the skin faced feed (SFF) and skin faced draw (SFD) modes of operation, and the arrangement of co-current and counter-current flows are listed in Table 1. The boundary conditions include symmetry, outlet, wall, convective flux and no-flux (i.e., impermeable boundary) as defined in [26]. The inlet channel concentrations were based on reported experimental FO data [9,16,29] that served as the basis for the present test cases.

The water flux (across the active FO membrane layer), J_w, is expressed by,

$$J_w = A(\pi_d - \pi_f) \tag{4}$$

in which π_d and π_f are the osmotic pressures at the active membrane layer surfaces at the draw and feed sides, respectively, and A is the intrinsic membrane water permeability coefficient. Within the context of the present work the terminology of "Intrinsic" membrane properties refers to membrane transport parameters for water and salt species (A and B, respectively), extracted from experimental data based on the CFD model accounting for concentration polarization. In other words, these A and B are the transport coefficient that multiply the osmotic pressure difference and concentration difference, between the active membrane surfaces on the draw side and the feed-side, to obtain the water and solute fluxes, respectively. Accordingly, the feed and draw solutes fluxes are specified by

$$J_i = B_i(C_{f,i} - C_{d,i}) \tag{5}$$

where $i = s$ or a for the feed salt and draw solute, respectively, B_i is the feed or draw solute permeability, and $C_{f,i}$, $C_{d,i}$are the respective species concentrations on the active membrane layer surfaces at the feed and draw sides, respectively.

Eqs. (1)–(5) and Table 1 define the 2-D DO desalination model (Fig. 1) with two different solutes in the feed (e.g. NaCl) and in the draw (e.g., NH_4HCO_3) channels for operation in either the SFF or SFD modes both in either the co-current and counter-current cross flow configurations. Numerical simulations with the current model require channel geometrical parameters (Fig. 1), solution properties (dynamic viscosity (η), density (ρ) and osmotic pressure (π)), mass diffusivity of the different solutes (D), solute membrane permeability coefficients (e.g., B_s, B_a and B_k for NaCl and NH_4HCO_3 and KCl, respectively), membrane water permeability A and thickness, hydraulic permeability (κ) and porosity (ε_p) of the porous support.

2.3. Model simulations

The model equations (Sections 2.1 and 2.2) were solved via the finite-element approach [26] for specific test cases (Tables 2 and 3) based on laboratory membrane geometries reported in the literature [4,30,29] and for a 1 m long channel that is of the order expected in commercial FO deployment [31]. The ratio of the feed and draw channels depth to length, d/L, is typically $o(10^{-2})$ in FO studies [32] and $o(10^{-4})$ in long membrane elements [33]. For all cases, the mesh density was increased from the bulk toward the membrane surfaces, with elements density set at ~120 elements/mm^2 in proximity of the membrane surface. Grid size independence was evaluated for all simulations to ensure solution convergence as described in [13], whereby global convergence was ascertained when the calculated water flux did not significantly change ($<0.01\%$) upon doubling the mesh density. Also, model predictions for the classical solution for the problem of a dissolving wall compared well with the classical analytical Lévêque solution (Appendix A6).

Table 2
Dimensions and cross flow velocities used in the simulations[a].

Ref. #	h_f, mm	h_d, mm	h_s, μm	v_f, cm s^{-1}	v_d, cm s^{-1}	L, cm	W, cm
[4]	1.75	1.75	50	15	15	14.6	9.5
[30]	3	3	40	8.5	8.5	7.7	2.6
[29]	3	0.25	100	0.563	6.76	14.8	7.7
Long channel	0.6	0.6	100	6.76	6.76	100	100

[a] h_f, h_d – feed and draw channel heights; h_s – support layer thickness; v_f, v_d – cross flow velocities in feed and draw channels, respectively; L – channel length; W – channel width.

In order to explore FO behavior in long relative to short channels, model simulations were first carried out to extract reasonable values of solute and water membrane permeabilities based on published experimental studies (Table 3) for FO operation [4,30,29] with either pure water or aqueous NaCl solution as the feed and with two different draw salts (NH_4HCO_3 and KCl). The first experimental dataset [4] was for FO experimental unit operated in counter-current operation with the membrane skin layer facing the feed solution (SFF mode). The second experimental dataset was for co-current FO operation with NaCl feed and KCl draw solute [30] with the membrane skin layer facing the feed (SFF). The third dataset [29] was for co-current FO operation, with NaCl feed and NH_4HCO_3 as draw solute support with the membrane active skin layer facing the draw solution (SFD mode). Intrinsic membrane water (A) and solute (B_i, the index i is for either KCl or NH_4HCO_3 draw solutions) were determined for each of the above FO case studies by fitting model predictions to reported experimental water and solute flux data. It is noted that one should distinguish between the above intrinsic and apparent water (A_b) and salt (B_b) transport coefficients. The latter reflect the overall (but not intrinsic) membrane transport resistance and include the additional resistance due to concentration polarization, while the former does not. Therefore, when the apparent coefficients are utilized, the water and solute fluxes (salt or draw solute) are expressed as

$$J_w = A_b(\pi_{db} - \pi_{fb}) \text{ and } J_i = B_{b,i}(C_{fb,i} - C_{db,i}) \tag{6}$$

in which π_{db} and π_{fb} are the bulk feed and draw solutions osmotic pressures, respectively, and $C_{b,i}$ and $C_{db,i}$ are the feed salt or draw solute (designated by subscript i) bulk concentrations in the feed and draw channels, respectively.

Using the present FO model, simulations were carried out for a long membrane channel (1 m), using the transport coefficients extracted from experimental studies with short bench-scale FO units. These simulations served to assess: (a) the degree of driving force decline (due to the coupled effect of concentration polarization), and (b) cross-migration of salts (across the membrane) and accordingly the impact on the achievable recovery. Simulations were carried out with solution properties (Section 2.3; and Appendices A1–A4) that were obtained either from the corresponding literature studies [4,29,30] or calculated as a function of salt concentration using a multi-electrolyte solution properties simulator (Appendices A1–A4). Data on permeability (κ) of FO membrane supports (used in Eq. (2)) are scarce, and thus Darcy's permeability coefficient for the FO support was estimated, based on RO support hydraulic permeability reported in [34], $\kappa = 2.34 \times 10^{-15}$ m^2 as an average value. Likewise support porosity (ε_p) is often not measured nor reported in FO studies, but FO supports porosity and tortuosity have been reported in the range of $\varepsilon_p = 0.35$–0.77, and $\tau = 1.7$ respectively [35,24,39]. Thus, reasonable mid-range values of $\varepsilon_p = 0.56$ and $\tau = 1.7$ were utilized in the present test cases, along with support thickness of $t_s = 40$, 50 and 100 μm in

Table 3
Apparent and intrinsic membrane transport parameters[a] based on reported experimental FO data.

Ref. #	C_f, [M] Feed salt: NaCl		C_d[b] [M]	$A \times 10^{12}$ m s^{-1} Pa^{-1}	$A_b \times 10^{12}$ m s^{-1} Pa^{-1}	B 10^{-8} m s^{-1}	B_b 10^{-8} m s^{-1}	J_w μm s^{-1}
[4]	0 (DI water)		Draw salt: NaCl					
		i	0.306 (0.288)	1.320	1.240	7.60	7.14	1.73
		ii	0.602 (0.548)	1.050	0.957	6.25	5.68	2.68
		iii	0.869 (0.770)	0.921	0.806	5.61	4.98	3.38
			Draw salt: NH_4HCO_3					
		iv	0.3188 (0.302)	1.147	1.086	13.64	12.9	1.52
		v	0.668 (0.622)	0.779	0.729	10.29	9.575	2.04
		vi	1.055 (0.957)	0.740	0.679	7.570	6.861	2.85
			Draw salt: KCl					
		vi	0.314 (0.296)	1.40	1.33	8.56	8.07	1.87
		vii	0.630 (0.574)	1.16	1.08	7.99	7.27	3.02
		vii	0.943 (0.840)	0.981	0.89	6.79	6.04	3.74
[30][c]	0.0856		Draw salt: KCl					
		i	0.5 (0.495)	0.656	0.620	[b]		1.18
		ii	1 (0.984)	0.591	0.560	B_{NaCl}=6.49		2.35
		iii	1.5 (1.445)	0.527	0.514	B_{KCl}=7.78		3.34
		iv	2 (1.922)	0.462	0.427			3.77
		v	3 (2.814)	0.333	0.326			4.42
[29][c]	0.5		Draw salt: NH_4HCO_3					
		i	1 (0.98)	0.531	0.367	[b]		0.537
		ii	2 (1.881)	0.295	0.224	B_{NaCl}=6.49		0.991
		iii	3 (2.655)	0.235	0.188	$B_{NH_4HCO_3}$ = 10.5		1.26
		iv	3.6 (3.099)	0.219	0.178			1.395

Note: A values were determined with a deviation of ~1.6% for the FO studies involving KCl and below ~1% for the experiments involving NH_4HCO_3. The estimated deviation for the extracted B coefficients were < 1%.

[a] The intrinsic A and B values were determined from fitting CFD model flux prediction to reported experimental data (Section 2.3; Tables 2 and 3) and their variability with draw solute concentration (at the membrane surface on the draw channel-side) is provided in Appendix A4. The A and B values in Table 3 are axially averaged values (along the membrane surface).

[b] Average draw solute concentrations at the membrane surface (draw channel-side) are given in parentheses along with the draw-solute feed concentration.

[c] In the absence of solute flux data in [30,29] B values for feed (NaCl) and draw (NH_4HCO_3, KCl) solutes were estimated from [4] for use in the case studies with system configurations and solution concentrations in [30,29]; all solutions were at 25 °C, but 30 °C in [29].

the analysis of FO data reported in [30], [4] and [29], respectively, corresponding to values of the support layer structural parameter (i.e., $S=t_s\tau/\varepsilon$) of 154, 192, and 384 μm, which is within the range reported in the literature [25,18]. It is acknowledged that the specific quantitative results, obtained from simulations for long membranes, will depend on the particular intrinsic membrane parameters (i.e., A and B) for the target FO system. Notwithstanding, the present modeling approach is expected to portray the expected FO transport behavior, without a loss of generality, for the various FO configurations.

3. Results and discussion

3.1. Intrinsic membrane permeability and salt transport coefficient

The FO model was initially utilized to extract intrinsic membrane transport parameters (Section 2.3) from published experimental data for short FO channels to enable subsequent evaluation of FO operation in long channels. A summary of the dimensions and cross flow velocities is provided in Table 2.

Comparison of the variation of membrane water permeability (A) for FO studies with cellulose triacetate (CTA) membranes and NH_4HCO_3 [4,29] and KCl [4,30] as the draw solutes are provided in Table 3. It is clear that both the apparent (i.e., based on the reported experimental flux and bulk osmotic pressure driving force) and intrinsic values of A and B (Eqs. (4) and (5)) decrease with increasing draw solute concentration (in the draw solution) (Table 3; Appendix A4); this behavior is consistent with the rise in water flux (with increasing draw solution concentration) which which in turn results in higher salt concentration at the membrane surface. In fact, inspection of the available experimental data [4,36,30,29] reveals that both A_b and B_b decrease with the draw solution concentration (Table 3; Appendix A4), and a similar trend is observed for the intrinsic A and B parameters. The above behavior is not surprising given that the water flux increases non-linearly with the draw solute concentration, reaching a plateau at high concentrations [37]. The concentration dependence of B is consistent with both experimental and theoretical conclusions [38] that the salt permeability coefficient is a strong non-linear function of solution concentration.

For the case studies evaluated in the present work (Table 3), the intrinsic A was found to be higher relative to A_b by 5.6–9.0% and 23–45% over the corresponding ranges of NH_4HCO_3 draw solution concentrations of 0.3–0.9 M, 0.5–3 M. The intrinsic A was also higher by 2.1–5.8% for the concentration range of 0.75–3.5M for KCl as the draw solute. The higher A relative to reported apparent coefficient (A_b) values should be expected, given that the actual osmotic pressure driving force (i.e., based on concentrations at the active membrane surface) is reduced by the CP layers on both sides of the membrane. The intrinsic salt transport coefficient B (Eq. (5)) extracted from [4] (see Appendix A4), which reported NaCl salt fluxes for FO with CTA type membrane, was also found to decrease (by 30%) with increasing draw solute concentration from 0.869 to 1.06 M (Table 3). Overall, analysis of experimental FO results from [4], for either NH_4HCO_3 or KCl as draw solutes, revealed A values that decreased by 35% and 30%, respectively, for the corresponding draw solute concentration ranges of 0.32–1.06 M and 0.314–0.943 M. Intrinsic draw solute membrane permeability (also extracted from [4]) of NH_4HCO_3 decreased by 44% over the range of its respective draw concentration of ~0.32–1.06 M (Appendix A4). It is plausible that the observed dependence of the membrane transport parameters on draw solute concentration may reflect non-idealities with respect to increased permeation resistance associated with draw salt back diffusion (i.e., from draw side to the feed side), in opposite direction to the water flux, which affects the actual internal permeation driving force and

the impact of opposing water and solute fluxes. It is important to note that experimental determination of membrane transport parameters in the RO mode (i.e., using fresh water in the feed side), where the feed channel is under significant hydraulic pressure, do not reproduce the transport conditions under FO operation. In such experiments any impact of solute concentration on the calculated permeability coefficient is likely to be masked by the dominance of the transmembrane pressure. Therefore, it should not be surprising that data from FO experiments would reveal variability of membrane transport parameters (A and B) with salt concentration. Clearly, more detailed experimental data on cross solute migration and transport parameter characterization are warranted in order to elucidate the above experimental observations. However, it is important to note that solute fluxes are not always reported in FO studies or not reported for a sufficient range of draw solute concentrations. Nonetheless, for high level of FO membrane rejection a significant impact of B on water flux is not expected. For example, increase of the highest B value listed in Table 3 by 100%, would be reflected by a reduction in A by less than ~0.21%. Therefore, in investigating FO behavior for the different configurations considered (Tables 2 and 3), the B values extracted from [4] were utilized (Appendix A4) as an approximation given the minor impact of B on water flux.

3.2. FO performance for a long membrane element

Transport behavior in a long (1 m) FO membrane element was simulated for aqueous feed NaCl and draw KCl and NH_4HCO_3 solutions, with corresponding channel heights both being 0.6 mm. These channel dimensions are consistent with the range reported for commercial spiral-wound RO membranes [31]. Simulations were carried out at the same conditions as in [30,29] (Section 3.1, Table 2) and with solution properties as a function of solute concentration along with membrane water permeability and solute transport parameters (Appendices A1–A3) extracted from [4] (as described in Section 3.1). Typical velocity and concentration fields in a long FO element are shown in Figs. 2 and 3, respectively, for inlet concentrations of 0.5 M NaCl feed and 3.5 M NH_4HCO_3 draw solutions, in a co-current SFD operation. As expected, the cross flow velocity decreases in the feed channel and increases in the draw channel as the respective channel exits are approached. The traverse velocity (i.e., permeate flux), across the support and membrane, decreases in the axial direction (as one moves away from the inlet region) which is consistent with the decreased osmotic pressure driving force as is evident in the concentration field depicted in Fig. 3. Indeed, the concentration fields for NaCl and NH_4HCO_3, across both channels and support, demonstrate growth of the concentration polarization layer for NaCl on the feed side and the dilutive concentration polarization layer for NH_4HCO_3 on the draw side. In the above example, the concentration of NH_4HCO_3 at the membrane surface at the (draw) channel exit is reduced, primarily due to the dilutive effect of water permeation from the feed side, by about 10% relative to channel inlet. At the same time, NaCl concentration in the draw channel, albeit low, rises up to ~11 mM (or 0.19 mg L^{-1}) at the membrane surface in the exit region. In the feed channel, NaCl concentrations at the support-bulk solution interface and at the membrane surface increase by about 7.4% and 5%, respectively, relative to the feed channel inlet concentration.

Due to draw solute cross migration, NH_4HCO_3 concentration at the membrane surface, in the feed channel, increases up to 0.2 M (for operation at draw solute feed inlet concentration of 3.5 M). Maximum decline in solute concentrations across the support layer as depicted in Fig. 3 is about 70 [mM] NH_4HCO_3 and about 20 [mM] NaCl. The draw solute concentration difference across the membrane decline is about 13% over the FO element length, while NaCl concentration difference across the membrane decreases by 5% as the feed flows from the entrance to the exit regions. It is noted that there is cross contamination of the draw stream by the feed solute (i.e., NaCl) and feed stream by the draw solute (i.e., NH_4HCO_3) reaching respective concentrations in the range of 200–230 ppm and 600–2700 ppm. This contamination level may present a challenge from the viewpoint of purification of the product water and the feed concentrate prior to subsequent use and possibly discharge of these two streams, respectively.

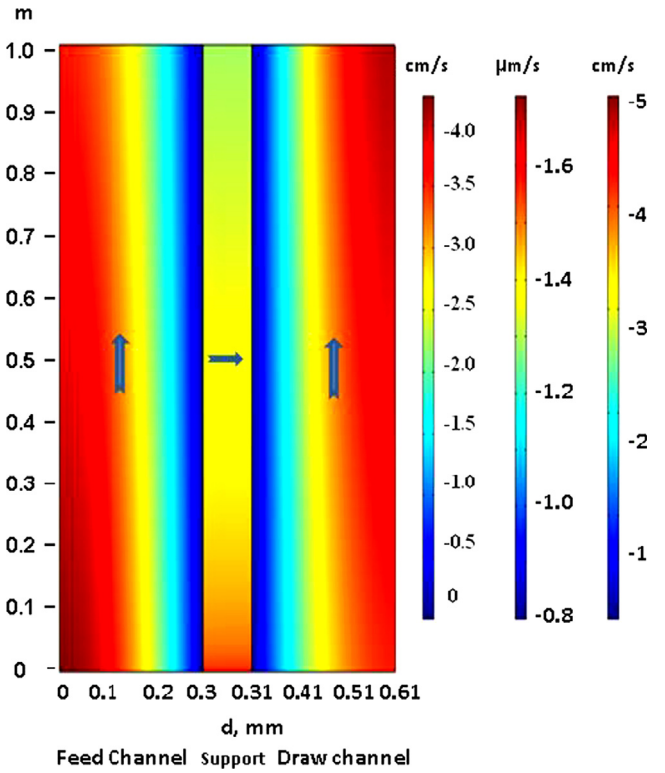

Fig. 2. Velocity map for co-current FO operation in 1 m long unit composed of feed (left) and draw (right) channels (only half-channel is shown in each side) with NaCl (**0.5 M**) and NH_4HCO_3 (**3 M**) as the feed and draw solutes, respectively. The channels are each 0.6 mm in thickness with 0.01 mm thick support layer, and where the active membrane area faces the draw channel (SFF mode).The simulation was based on FO conditions reported in [29] (Tables 2 and 3) with cross flow velocity of 2.82 cm s^{-1} (Re=42) taken to be the same in both channels (Table 2). The figure is in non-proportional dimensions in order to clarify the regions in the vicinity of the active membrane layer. For clarity of presentation, the support layer thickness is expanded 10-fold relative to the horizontal dimensions. The left concentration scale for each of the two figures is for the feed-side and the porous support region, while the concentration scales to the far right of each of the two figures are for the draw channel. Note: The white and black arrows indicate the solution flow and water flux directions, respectively.

3.3. Comparison of FO in a short (bench-scale) relative to long membrane elements

Comparison of transport behavior between short (14.8 cm, Table 2) bench-scale plate-and-frame and long (1 m) FO elements (Section 3.1) was conducted in order to assess the relevance of experimental results from the former, with respect to salt cross-migration and water flux, relative to the expected behavior for the latter. The short channel dimensions were as reported in [29] (Section 3.1, Table 2) and for the long channel as specified in Section 3.2 (Table 3). Simulations for co-current operation (Figs. 2 and 3) depict the growth of the dilutive draw CP and concentrative feed CP layers axially along the channel; thus, on the average, thicker concentration boundary layers are expected in the longer element. As a result, reduced water flux and more pronounced cross-migration salt fluxes are expected as shown in the example of Fig. 4. Overall, however, a higher recovery should be attained for longer FO elements or for a series of membranes in a single module as is the case in RO desalting. In this regard, it is noted

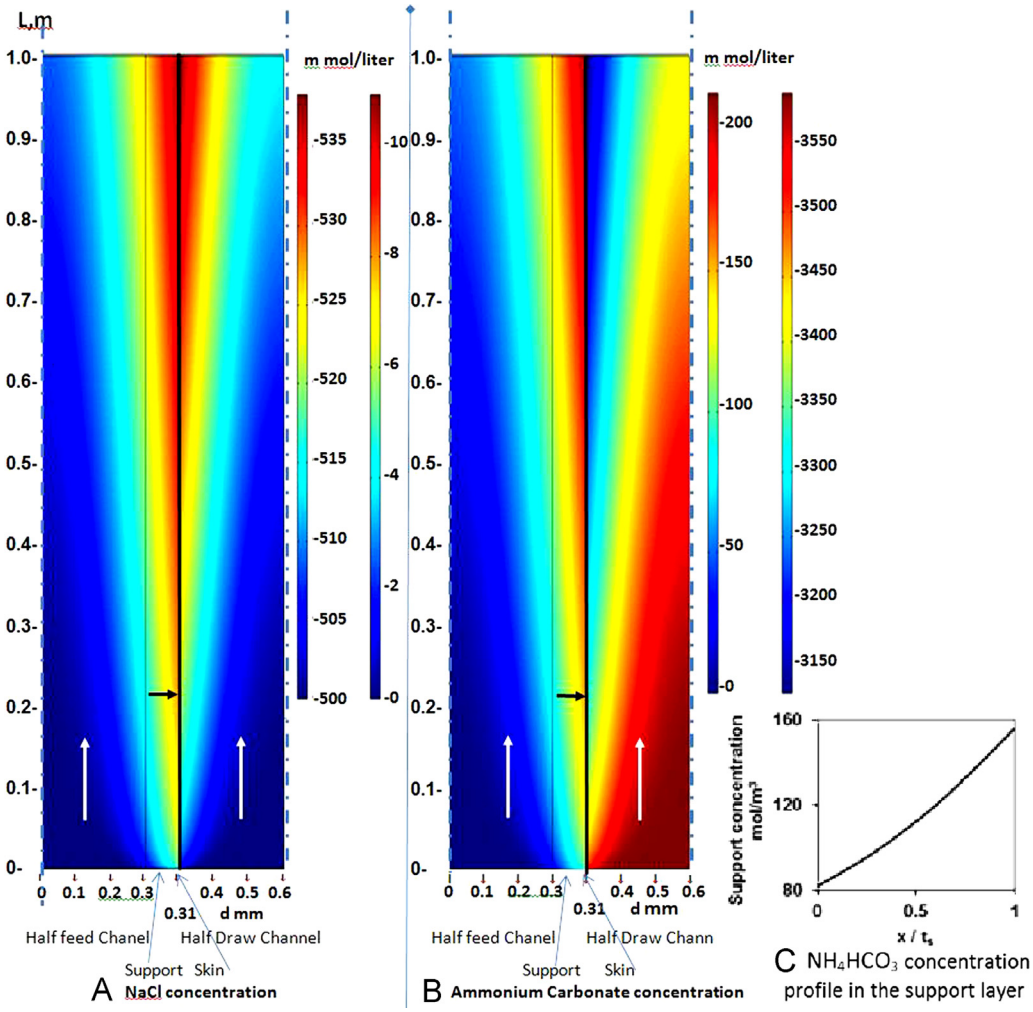

Fig. 3. Concentrations maps for NaCl (Left) and NH_4HCO_3 (Right) for co-current FO operation in 1 m long unit composed of feed and draw channels (only half-channel is shown in each side) that are 0.6 mm in thickness and 0.01 m thick support layer, with the active membrane facing the draw channel (SFF mode). Simulation conditions are as indicated for Fig. 2. The figure is in non-proportional dimensions in order to enlarge the regions in the vicinity of the active membrane layer. For clarity of presentation, the support layer thickness is expanded 10-fold relative to the horizontal dimensions. The left concentration scale for each of the two figures (A and B) is for the feed-side and the porous support region, while the concentration scales to the far right of each of the two figures are for the draw channel. Note: The white and black arrows indicate the solution flow and water flux directions, respectively. Inset (C) NH_4HCO_3 concentration profile at 0.3 m from the inlet section across the support layer thickness of t_s.

that previous studies reported that FO operation in the counter-current cross flow and SFD configurations is somewhat more efficient given the ability to maintain a more even driving force (and higher on the average) relative to other combinations of co-current/SFF or SFD modes, and the counter-current/SFF mode [1,13].

In order to illustrate FO performance under counter-current FO operation a simulation was carried out for the case of 0.5 M NaCl feed and 3.6 M NH_4HCO_3 draw solutions. The results demonstrated water and feed solute fluxes that increased, relative to co-current FO operation, by about 3% and 8%, respectively, while the draw solute flux (from the draw-side to the feed side) decreased by 13%. These results are consistent with previous work in which the preferred FO configuration was shown to be that of counter-current flow [2,13,40]. The above behavior is not surprising as it is well known in the field of heat-exchangers and separation processes that counter-current operation is more efficient than co-current operation. However, the advantage of counter-current operation decreases relative to co-current operation as the difference in the driving force between inlet and outlet of the separation module decreases. Although counter-current FO operation leads to only slight improvement in water flux, the cross migration of feed and draw solutes is a more significant reason for favoring counter-current operation.

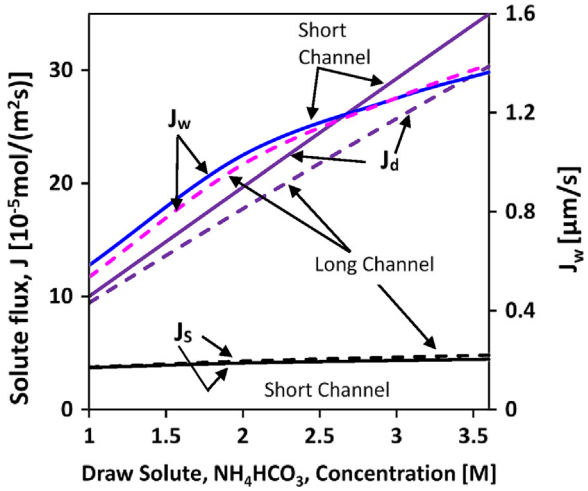

Fig. 4. Variation of fluxes of water, draw (NH_4HCO_3) and feed (NaCl) salts, for counter-current FO operation in short and long membrane channels, with draw solute feed concentration. The simulations are based on the FO operation for short and long channels with conditions of [29] listed in Tables 2 and 3 for 0.5 M NaCl feed concentration.

The achievable recovery (R) can be quantified from results of the CFD simulations as

$$R = \frac{Q_p}{Q_f} \times 100 = \frac{W \int_0^L J_w dy}{Q_f} 100 \quad (7)$$

where Q_p and Q_f are the feed and permeate flow rates, respectively, and L and W are the channel length and width, respectively. As shown in Fig. 5, for NH_4HCO_3 draw solution concentration in the range of 1–3.6 M and NaCl feed solution of 0.5 M, the attained recovery was a factor of ~5.8 fold higher for the long channel which was 6.8 times longer than the short (14.8 cm; Table 3) channel. In the longer channel the recovery is higher, and CP level of feed solute (NaCl) along the membrane (feed channel) rises to a great extent relative to the behavior observed in short experimental channels (for the same hydrodyanmic and feed/draw solution concentrations). Therefore, one would expect a greater level of salt leakage from the feed to draw channel. Also, greater leakage of draw solute (to the feed side) could be encountered with increased membrane channel length which may be reduced, to some extent due to dilution (on the draw side), with icnreased recovery. Leakage of (or cross-migration) of draw solute and feed salt can have a profound impact on the quality of the product water and feed-side concentrate stream composition. Therefore, it is important to assess salt cross-migration for channel lengths that are sufficiently long so as to provide a closer representation of the expected behavior in commercial FO elements.

The effect of leakage of salt and draw solutes can be quantified in terms of the respective solute concentrations in the streams exiting the draw and feed channels, calculated based on the axial profile of water and solutes fluxes, as expressed below

$$(C_i)_{exit,j} = \frac{M_i \int_0^L J_{i,j} dy}{\left[\int_0^d \rho_j v_j dx\big|_{y=L} \pm \int_0^L \rho_w J_w dy\right]} \quad (8)$$

where $(C_i)_{exit}$ is the exit mass concentration of the feed salt ($i=s$, i.e., NaCl) or draw solute ($i=a$, i.e., NH_4HCO_3) in the exit of channel j ($j=s$ feed channel, $j=a$ draw channel), M_i is the solute molecular weight, J_i and J_w are the solute and water, respectively, v_j is the inlet cross flow velocity in the designated channel, and where the "+" or "−" before the second integral in the denominator of Eq. (8) is for the calculation of the designated solute concentration in the exit of the draw or feed channels, respectively. Finally, ρ_j and ρ_w are the densities of the solution (in the inlet to the feed ($i=s$) or draw ($i=a$) channels) and of the permeate stream, respectively. An illustration of leakage of NH_4HCO_3 to the feed channel and NaCl to the draw channel is given in Fig. 6, for the permeability coefficients (B_a and B_s) discussed in Section 3.1 and channel geometries in Fig. 5, for a feed NaCl concentration of 0.5 M.

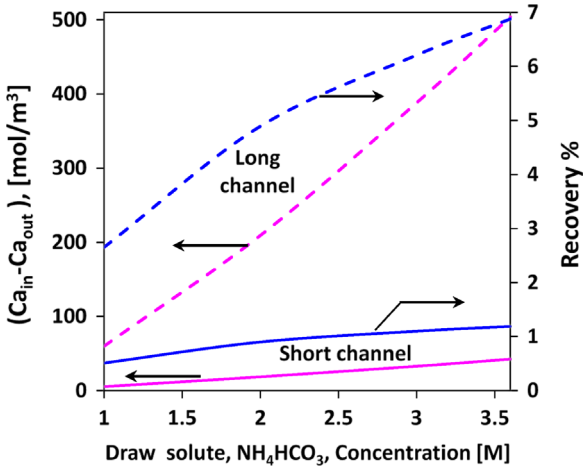

Fig. 5. Comparison of water recovery and draw solute (NH_4HCO_3) concentration change from the draw channel inlet to outlet for short versus long FO membrane units. The simulations as in Fig. 4 are based on the FO operation for short and long channels with conditions of [29] listed in Tables 2 and 3 for 0.5 M NaCl feed concentration.

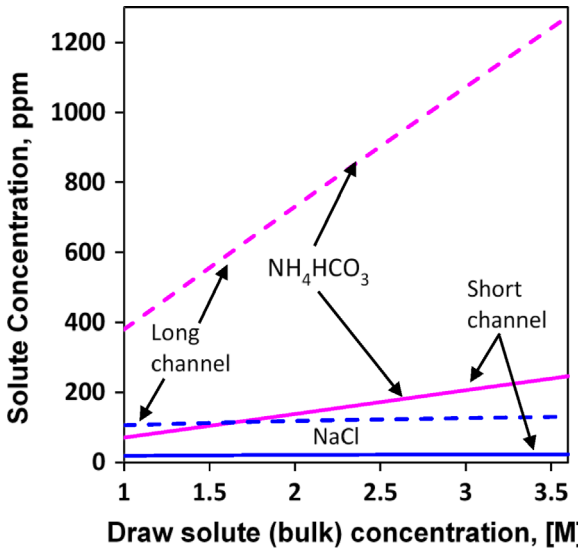

Fig. 6. The effect of cross-migration of feed salt (NaCl) and draw solute (NH_4HCO_3), for counter-current FO operation in short and long channels, quantified in terms of the average concentrations of these solutes at the exit of the feed and draw channels, respectively. Simulations conditions were for the simulations presented in Figs. 4 and 5.

Leakage of both solutes increases with increasing draw solute concentration. However, NH_4HCO_3 leakage from the draw to the feed channel is more significant than NaCl leakage to the draw side. For the simulation conditions ([29], Table 2), the resulting NH_4HCO_3 concentration in the stream exiting the long feed channel (0.38–1.28 kppm) was a factor of 5.3 greater relative to the short channel (14.8 cm) for the draw solute concentration range of 1–3.6 M. It is also noted that NH_4HCO_3 leakage increases nearly linearly with draw solute concentration. This flux increase is expected since higher draw solute concentration (and thus higher driving force; Fig. 4) and greater draw solute membrane permeability (B_a), relative to NaCl, result in a higher diffusional cross-migration flux. However, the degree of NaCl leakage is impacted only slightly by the draw solute concentration since NaCl cross-migration is governed by its feed-draw channels concentration driving force; the slight increase in NaCl leakage (Fig. 6) is attributed to the increasing permeate water flux with draw solute concentration.

4. Conclusions

Forward osmosis desalination was investigated using a 2-D CFD model of the fully-coupled hydrodynamics and both feed salt and draw solute mass transfer equations. The model was developed for a detailed composite channel structure (feed and draw channels, membrane skin layer and porous support) that can incorporate four different configurations of FO operation where the membrane skin faces the salt feed solution (SFF mode) or where the membrane skin faces the draw solution (SFD) with either co-current or counter current cross flow velocities. FO operation in the counter-current/SFD mode is preferred since it provides (slight) improvement in water flux and significantly lower cross migration of feed and draw solutes relative to FO operation in the co-current FO mode. Model analysis of reported experimental FO data, from short laboratory FO units (order of ~10 cm), revealed that membrane and solute permeabilities decreased with draw solute feed concentration. Comparison of FO performance for short relative to long (order of ~1 m) FO channels,

based on the intrinsic transport coefficients (i.e., A and B) extracted from experimental data, demonstrated nearly identical water and feed salt fluxes, but somewhat higher (up to ~9%) draw solute flux (from draw to feed channel). As expected water recovery was significantly higher (by up to a factor of 5.3) in the long channel and with significant leakage (across the membrane) of both salt and draw solutes which was more pronounced for the long FO channel. As a consequence, draw and salt concentrations in the feed and draw exit streams, respectively, can be significantly higher (possibly up to an order of magnitude) in long relative versus short (bench-scale) FO channels. Overall, the present study suggests that assessment of FO performance in long channels, as can be derived from CFD modeling based on experimentally derived membrane transport parameters, may be essential for full-scale plant design in order to minimize salt leakage, optimize recovery, and for setting accurate inlet/outlet conditions to enable simulations of membrane elements in series.

Acknowledgments

This research was supported by Grant no. 2014337 from the United States–Israel Binational Science Foundation (BSF). P. Christofides, Y. Cohen and A. Zhu also acknowledge support from the California Department of Water Resources and the National Science Foundation Grant No. 0963183. Also acknowledged is assistance of Dr. Anditya Rahardianto with determination of solution physicochemical and transport properties.

Appendix. Solution and solute properties and membrane transport parameters

A1. NaCl solution properties and solute diffusion coefficient

NaCl solution parameters (density ρ, dynamic viscosity η, osmotic pressure π) and solute diffusivity, D needed for analysis of FO system from [30,29] were extracted from the database/OLI Stream Analyzer 3.2 (OLI Systems Inc., Stream Analyzer 3.2, 2012; Morris Plains, NJ). Dependence of the above parameters on NaCl concentration, C [mM], was expressed via the following empirical expressions,

At 25 °C	
$\rho = 996.845 + 0.0405C$	(kg m^{-3})
$\eta = 8.907\times10^{-4} + 7\times10^{-8}C + 1.75\times10^{-11}C^2$	(Pa s)
$\pi = 4260C + 0.7C^2$	(Pa)
$D = 1.57\times10^{-9} - 3.6\times10^{-13}C + 3\times10^{-16}C^2$ (for $C < 528.37$)	(m s^{-1})
$D = 1.458\times10^{-9} - (C-528.37)\times 10^{-13} - (C-528.37)^2\times 6\times10^{-18}$ (for $3496 > C \geq 528.37$)	(m^2 s^{-1})
At 30 °C	
$\rho = 995.404 + 0.04C$	(kg m^{-3})
$\eta = 7.981\times10^{-4} + 6.4\times10^{-8}C + 1.6\times10^{-11}C^2$	(Pa s)
$\pi = 4280C + 0.71C^2$	(Pa)
$D = 1.78\times10^{-9} - 7\times10^{-13}C + 1.5\times10^{-15}C^2 - 1.2\times10^{-18}C^3$ (for $C < 315.51$)	(m^2 s^{-1})
$D = 1.67\times10^{-9} - (C-315.51)\times 1.19\times10^{-13} - (C-315.51)^2\times 4\times10^{-18}$ (for $3496 > C \geq 315.51$)	(m^2 s^{-1})

Note: At NaCl concentration $C \leq 0.5$ M the van't Hoff formula (for ideal solution), $\pi = iCRT$ is applicable (where i, C, R, and T are the van't Hoff factor, NaCl concentration, gas constant and absolute temperature) and in agreement with the above empirical expression (for the indicated temperature) within a deviation of less than 2.1%.

A2. KCl solution properties and solute diffusion coefficient

KCl solution parameters (density ρ, dynamic viscosity η, osmotic pressure π) and solute diffusivity, D needed for analysis of FO data from [30] were extracted from the database/OLI Stream Analyzer 3.2. KCl concentration, C [mM], dependence of the above parameters was expressed by the following empirical relations:

$\rho = 997.048 + 0.048C + 1.04\times10^{-6}C^2$	(kg m^{-3})
$\eta = 8.46\times10^{-4} + 3.5\times10^{-12}C^2$	(Pa s)
$D = 1.88\times10^{-9} + 9\times10^{-14}C + 1.43\times10^{-17}C^2$	(m^2 s^{-1})
$\pi = 4500C + 0.047C^2$	(MPa)

A3. NH_4HCO_3 solution and solute properties

Transport parameters for the NH_4HCO_3 draw solution (density ρ, dynamic viscosity η, and solute diffusivity D) and its osmotic pressure π were obtained from the OLI database/OLI Stream Analyzer 3.2. NH_4HCO_3 concentration, C [mM], dependence of the above parameters was quantified via the following empirical relations:

At 25 °C	
$\rho = 996.84 + 0.031C - 1.2\times10^{-6}C^2$	(kg m^{-3})
$\eta = 8.971\times10^{-4} + 3.2\times10^{-7}C - 4.5\times10^{-12}C^2$	(Pa s)
$D = 1.429\times10^{-9} - 6.6\times10^{-14}C + 1.86\times10^{-16}C^2$ (for $C < 481.01$)	(m^2 s^{-1})
$D = 1.44\times10^{-9} + 1.06(C-481.01)$ $1.06\times10^{-13} + (C-481.01)^2\times10^{-17}$ (for $3111 > C \geq 481.01$)	(m^2 s^{-1})
$\pi = 4410C - 0.32C^2$	(Pa)
At 30 °C	
$\rho = 995.404 + 0.0305C - 1.18\times10^{-6}C^2$	(kg m^{-3})
$\eta = 7.981\times10^{-4} + 2.91\times10^{-7}C - 7\times10^{-12}C^2$	(Pa s)
$D = 1.608\times10^{-9} - 8.2\times10^{-14}C + 2.31\times10^{-16}C^2$ (for $C < 425.084$)	(m^2 s^{-1})
$D = 1.61\times10^{-9} + (C-425.08)$ $1.1\times10^{-13} + (C-425.08)^2\times9.5\times10^{-18}$ ($3120 > C \geq 425.08$)	(m^2 s^{-1})
$\pi = 4500C - 0.32C^2$	(Pa)

A4. Membrane intrinsic water permeability and salt transport coefficients

(1) Data: [4], feed salt concentration DI water and different draw solutes: NaCl, NH_4HCO_3 and KCl (Table 4) for FO studies with CTA membrane

Intrinsic membrane functions A's and B's extracted from reported experimental data in Table 4 of [4], for FO studies with CTA membrane, by matching with CFD model predictions. The A and B vary with the draw solute concentration, C[M], at the membrane surface. The A and B parameters were expressed via the following empirical expressions (the subscripts in the listed A coefficient denote the solute used in the draw-side),

$A_{NaCl} = (1.54–0.83C)\times10^{-12}$,	m s^{-1} Pa^{-1},	0.306 M $\leq C \leq$ 0.869 M
$B_{NaCl} = (8.68–4.1C)\times10^{-8}$,	m s^{-1},	0.306 M $\leq C \leq$ 0.869 M
$A_{KCl} = (1.631 - 0.788C)\times10^{-12}$,	m s^{-1} Pa^{-1},	0.314 $\leq C \leq$ 0.943 M
$B_{KCl} = (10.1–3.94C)\times10^{-8}$,	m s^{-1},	0.314 M $\leq C \leq$ 0.943 M
$A_{NH_4HCO_3} = (1.3–0.62C)\times10^{-12}$,	m s^{-1} Pa^{-1},	0.319 M $\leq C \leq$ 1.05 M

$B_{NH_4HCO_3} = (1.59-0.62C)\times 10^{-7}$ m s^{-1}, 0.319 M ≤ C ≤ 1.05 M

The concentration ranges are according to the data of [4] from which the intrinsic membrane transport parameters were derived. Parameter values outside the above concentration ranges were taken to be equal to the lower or upper limits of the correlating expression under consideration as the case applies. Intrinsic membrane permeability A as a function of draw solute concentration C (at the membrane surface) was determined based on analysis of the experimental data of [29] and [30] using the CFD model as described in Section 2.3.

(2) Data: [29], feed salt concentration 0.5 M NaCl, draw solute feed concentration range 1–3.6 M NH_4HCO_3, CTA membrane

Draw solute (NH_4HCO_3) concentration-dependence of membrane water permeability,

$A = 0.89 - 0.45C + 0.075C^2$ m s^{-1} Pa^{-1}, (1 ≤ C ≤ 3.6 M)

(3) Data: [30], feed salt concentration 0.0856 [M], NaCl, draw solute feed concentration: 0.5–3 M KCl, TFC-RO membrane

Draw solute (KCl) concentration-dependence of membrane water permeability,

$A = 0.72 - 0.133C$ m s^{-1} Pa^{-1}, (0.5 < C < 3 M)

A5. Supplementary illustrations of model results for laboratory FO channels

See Figs. A1 and A2.

A6. Comparison of CFD model predictions of the liquid-side mass transfer coefficient and the analytical Leveque solution for the wall-liquid diffusion problem

The present CFD model is based on solution of the fundamental equations of momentum and mass transfer for the FO system domain that consists of two channels separated by a membrane (on a porous support). While the CFD model provided excellent fit to experimental flux data from different literature sources, it is instructive to demonstrate the agreement of this fundamental model with the classical analytical Lévêque solution for mass transfer at an impermeable wall (*M.D. Lévêque, Les lois de la transmission de chaleur par convection, An Mines, 13:201 (1928)*). The Lévêque solution for the local fluid-wall mass transfer coefficient (*J. Zeman, A.L. Zydney, Macrofiltration and Ultrafiltration: Principles and Applications, pp. 359, Marcel Dekker, 1996*) is given below

$$k_f(y) = 0.538\left(\frac{D^2\gamma_w}{y}\right)^{1/3} \quad \text{(A6.1)}$$

in which y is the axial distance from the channel entry, D is the solute mass diffusivity and γ_w is the shear rate at the wall ($\gamma_w = 6v/h$, where v is the average axial velocity in the channel and h is the channel thickness). The average mass transfer coefficient, $\bar{k}_f$, is derived by averaging the local mass transfer coefficient from Eq. (A6.1) over the channel length, L, (i.e., $\bar{k}_f = (1/L)\int_0^L k_f(y)\,dy$) leading to

$$\bar{k}_f = 0.81\left(\frac{D^2\gamma_w}{L}\right)^{1/3} \quad \text{(A6.2)}$$

The local and average mass transfer coefficients as expressed by Eqs. (A6.1) and (A6.2) can be cast in terms of the local, $Sh(y)$, and average,

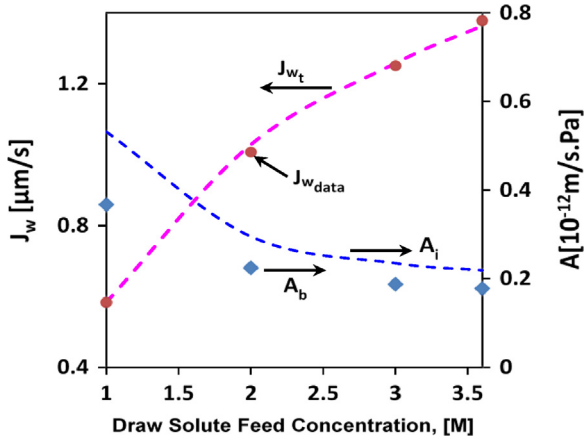

Fig. A2. Illustration of the model fit (J_w, dashed line) to reported FO water flux data (for co-current operation) from [29] for different NH_4HCO_3 draw solute feed concentrations. The extracted intrinsic water permeability coefficient (A) is shown by the dashed line, along with the apparent water permeability coefficient, A_b (filled circles), based on flux data (filled diamonds) reported in [29] (lowest graph in Fig. 2a of [29]). Feed salt concentration of 0.5 M NaCl with NH_4HCO_3 draw solution (concentration range of 1–4 M).

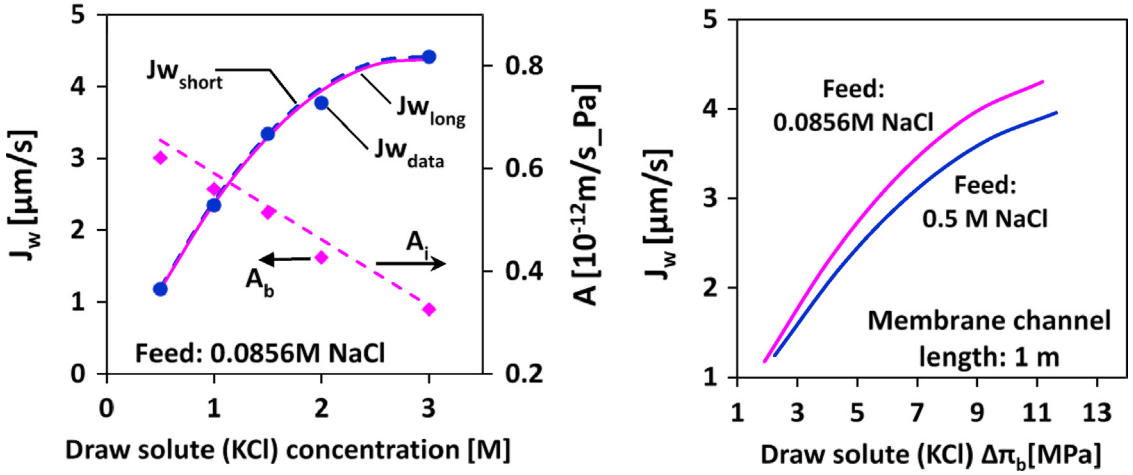

Fig. A1. (*Left*) Model fit to reported water flux data in Fig. 6a (DS25°C-BW25°C) of [30] for counter-current FO operation in a small FO unit with 0.0856 M NaCl feed and different KCl draw solute concentrations (Table 3). Extracted intrinsic water permeability coefficients, A (dashed line), are shown along with the apparent water permeability coefficient, A_b (diamonds) calculated from the reported flux data of [30]. The dashed line, $(J_w)_{short}$, represents model fit to experimental flux data (blue circles) of [30], along with simulation results for permeate water flux for a 1 m long channel (solid line). Feed salt solution concentration: 0.0856 M NaCl with KCl draw solute concentration range of 0.5–3 M. (*Right*) Water flux simulation results for a 1 m long membrane channel (FO configuration, draw solute concentrations and flow conditions as in [30] (Tables 2 and 3) for 0.0856 M and 0.5 M NaCl feed solution). (For interpretation of the references to color in this figure legend, the reader is referred to the web version of this article.).

$\overline{Sh}$, Sherwood numbers as given in Eqs. (A6.3) and (A6.4):

$$Sh(y) = \frac{k_f(y)h}{D} = 0.978\left[ReSc\left(\frac{h}{y}\right)\right]^{1/3} \quad \text{(A6.3)}$$

$$\overline{Sh} = \frac{\overline{k}_f h}{D} = 1.4674\left[ReSc\left(\frac{h}{L}\right)\right]^{1/3} \quad \text{(A6.4)}$$

in which Sc is the Schmidt number (i.e., $Sc = \nu/D$, where ν is the fluid kinematic viscosity) and Re is the Reynolds number ($Re = Vh/\nu$) defined based on the channel height, h.

As an illustration of the performance and applicability of the present model, the local mass transfer coefficient was determined for the experimental FO system of She et al. (*J. Membr. Sci. 401–402 (2012) 262–273*) in which an aqueous NaCl solution was used on the draw channel side with DI water on the feed channel side. The membrane geometry was set with *length* = 0.147 m, *width* = 0.095 m, support layer thickness, d = 0.86 mm, solute diffusivity, $D = 1.138 \times 10^{-9}$ m^2 s^{-1}, *cross flow velocity*, V = 0.085 m s^{-1} (set to be the same in both channels), 1 M draw solute concentration. Model simulations were carried out with the results then utilized to calculate the mass transfer coefficient on the draw-side. The mass transfer coefficient was determined from knowledge of the concentration profile where the thickness of the concentration boundary layer, δ, was taken to be the distance from the surface at which $C(x)/C_b = 0.99$. Accordingly, the local mass transfer coefficient was calculated from $k_f = J_s/(C_b - C_m)$), where C_m is the solute concentration at the membrane surface. Following the above, the mass transfer coefficients determined from the CFD model and based on the analytical Lévêque solution are compared in Fig. A3 in terms of the local Sherwood number.

The results show that the numerical and analytical Lévêque solutions for the local Sherwood number closely match with an average absolute percent deviation of 6.5%. It is stressed, that the Lévêque solution is an approximation (e.g., it approximates the velocity profile near the wall as linear, assumes fully developed flow field, and neglects water and solute permeation; see *E. Lyster, Y. Cohen, J. Membr. Sci., 303, 140–153, 2007*), which is suitable as a reasonable estimate depending on the specific application.

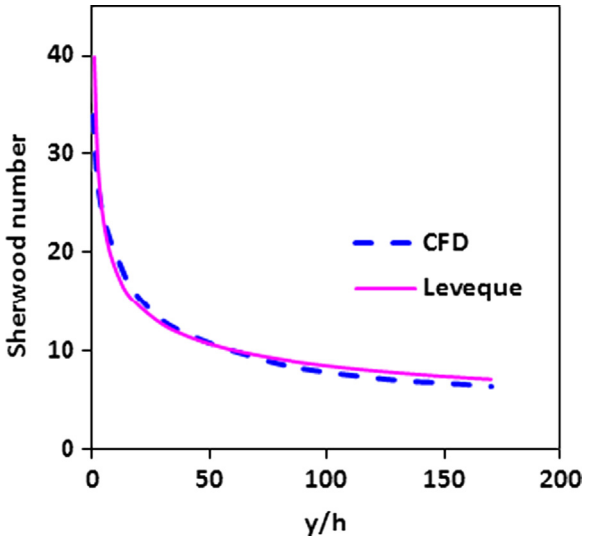

Fig. A3. Local Sherwood number for the draw solute on the draw channel side as determined from the CFD model and the Lévêque solution (Eq. (A6.1)) based on simulations for FO operation (Data source: *Q. She, X. Jin, C.Y. Tang, J. Membr. Sci. 401–402 (2012) 262–273*; Fig. 4). (Draw solute concentration: 1 M; Feed channel: DI water; Draw solute diffusion coefficient = 1.138×10^{-9} m^2 s^{-1}; channel height, h = 0.86 mm; Re = 76.5, Sc = 839).

Nomenclature

A	Water permeability coefficient [m s^{-1} Pa^{-1}]
B	Salt permeability coefficient [m s^{-1}]
C, c	Concentrations [M]
CP	concentration polarization
D	diffusivity [m s^{-1}]
d	Channel width [m]
ECP	External CP
FEM	Finite elements
FO	Forward osmosis
ICP	Internal CP
J	Flux, units of [mol m^{-2} s^{-1}] and [m s^{-1}] for salt and water fluxes, respectively
L	Membrane length [m]
p	Pressure
Q_f	Feed solution flow rate [m^3 s^{-1}]
RO	Reverse osmosis
SFD	Skin faced draw
SFF	Skin faced feed
T	Temperature [°C] or transpose
$\mathbf{u}$	Velocity vector (u, v) [m s^{-1}]
u,v	Velocities [m s^{-1}] along x and y coordinates, respectively
x, y	Coordinates in traverse direction and along the membrane length, respectively
2D	Two-dimensional

Greek letters

∇	Partial derivatives 2D vector ($\partial/\partial x$, $\partial/\partial y$)
ε	Porosity (volume fraction)
η	Dynamic viscosity [Pa s]
κ	Permeability of porous medium [m^2]
π	Osmotic pressure [Pa]
ρ	Solution density [kg m^{-3}]

Indices

a	NH_4HCO_3
d	Draw
f	Feed
in	Channel inlet
k	KCl
m	Membrane
out	Channel outlet
p	Porous support
s	Feed salt (e.g., NaCl)
w	Water

References

[1] R.W. Holloway, A.E. Childress, K.E. Dennett, T.Y. Cath, Forward osmosis for concentration of anaerobic digester centrate, Water Res. 41 (2007) 4005–4014.
[2] T.Y. Cath, A.E. Childress, M. Elimelech, Forward osmosis: principles, applications, and recent developments, J. Membr. Sci. 281 (2006) 70–87.
[3] O.A. Bamaga, A. Yokochi, E.G. Beaudry, Application of forward osmosis in pretreatment of seawater for small reverse osmosis desalination units, Desalin. Water Treat. 5 (1–3) (2009) 183–191.
[4] A. Achilli, T.Y. Cath, A.E. Childress, Selection of inorganic-based draw solutions for forward osmosis applications, J. Membr. Sci. 364 (2010) 233–241.
[5] S. Zhaoa, L. Zou, C.Y. Tang, D. Mulcahy, Review, Recent developments in forward osmosis: opportunities and challenges, J. Membr. Sci. 396 (2012) 1–21.

[6] P. Sherub, S.H. Kyong, H. Seungkwan, L. Sangyoup, V. Saravanamuthu, A novel low energy fertilizer driven forward osmosis desalination for direct fertigation: evaluating the performance of fertilizer draw solutions, J. Membr. Sci. 375 (1–2) (2011) 172–181.
[7] N. Hancock, T.Y. Cath, Solute coupled diffusion in osmotically driven membrane processes, Environ. Sci. Technol. 43 (2009) 6769–6775.
[8] S. Chou, L. Shi, R. Lei, C.Y. Wang, C. Tang, A.G. Qiu, Fane, Characteristics and potential applications of a novel forward osmosis hollow fiber membrane, Desalination 261 (3) (2010) 365–372.
[9] J.R. McCutcheon, M. Elimelech, Influence of concentrative and dilutive internal concentration polarization on flux behavior in forward osmosis, J. Membr. Sci. 284 (2006) 237–247.
[10] C.H. Tan, H.Y. Ng, Modified models to predict flux behavior in forward osmosis in consideration of external and internal concentration polarizations, J. Membr. Sci. 324 (2008) 209–219.
[11] A. Tiraferri, N.Y. Yip, W.A. Phillip, J.D. Schiffman, M. Elimelech, Relating performance of thin-film composite forward osmosis membranes to support layer formation and structure, J. Membr. Sci. 367 (2011) 340–352.
[12] A. Sagiv, R. Semiat, Modeling of backwash cleaning methods for RO membranes, Desalination 261 (3) (2010) 338–346.
[13] A. Sagiv, R. Semiat, Finite element analysis of forward osmosis process using NaCl solutions, J. Membr. Sci. 379 (2011) 86–96.
[14] A. Sagiv, N. Avraham, C.G. Dosoretz, R. Semiat, Osmotic backwash mechanism of reverse osmosis membranes, J. Membr. Sci. 322 (1) (2008) 225–233.
[15] V. Gekas, B. Hallstorm, Mass transfer in the membrane concentration polarization layer under turbulent cross flow. I. Critical literature review and adaptation of existing Sherwood correlations to membrane operations, J. Membr. Sci. 30 (1987) 153–170.
[16] J.J. Qin, S. Chen, M.H. Oo, K.A. Kekre, E.R. Cornelissen, C.J. Ruiken, Experimental studies and modeling on concentration polarization in forward osmosis, Water Sci. Technol. 61 (11) (2010) 2897–2904.
[17] J.S. Choi, H. Kim, S. Lee, T.M. Hwang, H. Oh, D.R. Yang, J.H. Kim, Theoretical investigation of hybrid desalination system combining reverse osmosis and forward osmosis, Desalin. Water Treat. 15 (1–3) (2010) 114–120.
[18] Y. Xu, X. Peng, C.Y. Tang, Q.S. Fu, S. Nie, Effect of draw solution concentration and operating conditions on forward osmosis and pressure retarded osmosis performance in a spiral wound module, J. Membr. Sci. 348 (2010) 298–309.
[19] D.H. Jung, J. Lee, D.Y. Kim, Y.G. Lee, M. Park, S. Lee, D.R. Yang, J.H. Kim, Simulation of forward osmosis membrane process: effect of membrane orientation, Desalination 277 (2011) 83–91.
[20] A. Sagiv, R. Semiat, Parameters affecting backwash variables of RO membranes, Desalination 261 (3) (2010) 347–353.
[21] B. Gu, D.Y. Kim, J.H. Kim, D.R. Yang, Mathematical model of flat sheet membrane modules for FO Process: plate-and-frame module and spiral-wound module, J. Membr. Sci. 379 (1–2) (2011) 403–415.
[22] M.F. Gruber, C.J. Johnson, L. Yde, C. Helix-Nielsen, Computational Fluid Dynamics simulations of flow and concentration polarization in forward osmosis membrane systems, J. Membr. Sci. 379 (2011) 488–495.
[23] M.F. Gruber, C.J. Johnson, C. Tang, M.H. Jensen, L. Yde, C. Helix-Nielsen, Validation and analysis of forward osmosis CFD model in complex 3D geometries, Membranes 2 (2012) 764–782.
[24] J. Wei, C. Qiu, C.Y. Tang, R. Wang, A.G. Fane, Synthesis and characterization of flat-sheet thin film composite forward osmosis membranes, J. Membr. Sci. 372 (2011) 292–302.
[25] M. Park, J.H. Kim, Numerical analysis of spacer impacts on forward osmosis membrane process using concentration polarization index, J. Membr. Sci. 427 (2013) 10–20.
[26] Comsol AB (Multiphysics 4.3a), Stockholm: 1998–2012.
[27] M. Gimmelshtein, R. Semiat, Investigation of flow next to membrane walls, J. Membr. Sci. 264 (2005) 137–150.
[28] V. Geraldes, V. Semião, M.N. Pinho, Flow management in nanofiltration spiral wound modules with ladder-type spacers, J. Membr. Sci. 203 (2002) 87–102.
[29] B.S. Chanukya, S. Patil, N.K. Rastogi, Influence of concentration polarization on flux behavior in forward osmosis during desalination using ammonium bicarbonate, Desalination 312 (2013) 39–44.
[30] S. Phuntsho, S. Vigneswaran, J. Kandasamy, S. Hong, S. Lee, H.K. Shon, Influence of temperature and temperature difference in the performance of forward osmosis desalination process, J. Membr. Sci. 415–416 (2012) 734–744.
[31] G. Schock, A. Miquel, Mass transfer and pressure loss in spiral wound modules, Desalination 64 (1987) 339–352.
[32] H.Y. Ng, W. Tang, W.S. Wong, Performance of forward (direct) osmosis process: membrane structure and transport phenomenon, Environ. Sci. Technol. 40 (7) (2006) 2408–2413.
[33] GE Sepa™ CF II Med/High Foulant System, GE Osmonics Laboratories, 1995–2010.
[34] R.P. Castro, Y. Cohen, H.G. Monbouquette, The permeability behavior of polyvinylpyrrolidonemodified porous silica membranes, J. Membr. Sci. 84 (1993) 151–160.
[35] S. Zhang, K.Y. Wang, T.S. Chung, Y.C. Jean, H. Chen, Molecular design of the cellulose ester-based forward osmosis membranes for desalination, Chem. Eng. Sci. 66 (9) (2011) 2008–2018.
[36] W.A. Phillip, J.S. Yong, M. Elimelech, Reverse draw solute permeation in forward osmosis: modeling and experiments, Environ. Sci. Technol. 44 (2010) 5170–5176.
[37] R.W. Field, J.J. Wu, Mass transfer limitations in forward osmosis: are some potential applications overhyped? Desalination 318 (2013) 118–124.
[38] A. Yaroshchuk, Influence of osmosis on the diffusion from concentrated solutions through composite/asymmetric membranes: theoretical analysis, J. Membr. Sci. 355 (2010) 98–103.
[39] M.F. Paugam, J. Buffle, Comparison of carrier-facilitated copper (II) ion transport mechanisms in a supported liquid membrane and in a plasticized cellulose triacetate membrane 147 (1998) 207–215J. Membr. Sci. 147 (1998) 207–215.
[40] D. Xiao, W. Li, S. Chou, R. Wang, C.Y. Tang, A modeling investigation on optimizing the design of forward osmosis hollow fiber modules, J. Membr. Sci. 392–393 (2012) 76–87.